

SpectralAdapt: Semi-Supervised Domain Adaptation with Spectral Priors for Human-Centered Hyperspectral Image Reconstruction

Yufei Wen, Yuting Zhang, Jingdan Kang, Hao Ren, Weibin Cheng,
Jintai Chen, and Kaishun Wu[†]

Abstract—Hyperspectral imaging (HSI) holds great potential for healthcare due to its rich spectral information. However, acquiring HSI data remains costly and technically demanding. Hyperspectral image reconstruction offers a practical solution by recovering HSI data from accessible modalities, such as RGB. While general domain datasets are abundant, the scarcity of human HSI data limits progress in medical applications. To tackle this, we propose SpectralAdapt, a semi-supervised domain adaptation (SSDA) framework that bridges the domain gap between general and human-centered HSI datasets. To fully exploit limited labels and abundant unlabeled data, we enhance spectral reasoning by introducing Spectral Density Masking (SDM), which adaptively masks RGB channels based on their spectral complexity, encouraging recovery of informative regions from complementary cues during consistency training. Furthermore, we introduce Spectral Endmember Representation Alignment (SERA), which derives physically interpretable endmembers from valuable labeled pixels and employs them as domain-invariant anchors to guide unlabeled predictions, with momentum updates ensuring adaptability and stability. These components are seamlessly integrated into SpectralAdapt, a spectral prior-guided framework that effectively mitigates domain shift, spectral degradation, and data scarcity in HSI reconstruction. Experiments on benchmark datasets demonstrate consistent improvements in spectral fidelity, cross-domain generalization, and training stability, highlighting the promise of SSDA as an efficient solution for hyperspectral imaging in healthcare.

Index Terms—Semi-Supervised Domain Adaptation, Hyperspectral Imaging, Spectral Reconstruction

I. INTRODUCTION

Hyperspectral imaging (HSI) has emerged as a pivotal technology in various fields, including geology, marine science, agriculture, forestry, hydrology, urban studies, and environmental science [1]–[3], owing to its ability to capture rich spectral information across a wide range of wavelengths. By revealing subtle biochemical and structural variations that are often imperceptible to conventional RGB or multispectral imaging, HSI has shown great promise in human health applications. In particular, it has demonstrated potential in enhancing disease diagnosis and physiological monitoring, with notable examples including cancer detection [4]–[6] and hemoglobin concentration estimation [7], [8].

Nevertheless, the acquisition of hyperspectral images (HSI) in health scenarios remains both time-consuming and costly, primarily due to the need for specialized imaging systems. In clinical settings, the deployment of such systems is often limited by factors such as hardware complexity, acquisition latency, and compatibility with real-time diagnostic workflows. Moreover, when human subjects are involved, additional ethical and regulatory constraints must be satisfied to ensure

patient safety and data confidentiality, further increasing logistical complexity and financial burden [10].

To address the high acquisition cost of hyperspectral imaging, researchers have proposed reconstruction-based methods that recover hyperspectral images from more economical measurement modalities, such as conventional RGB images or Coded Aperture Snapshot Spectral Imaging (CASSI) systems [11]–[13]. These approaches aim to significantly reduce the hardware and operational costs associated with hyperspectral acquisition, while preserving high spectral fidelity and spatial accuracy. Recent advances in this area have leveraged powerful deep learning architectures to further enhance reconstruction performance in terms of both accuracy and computational efficiency. Convolutional Neural Networks (CNNs) have been widely adopted in early works for their strong local modeling capacity [14]–[16], while more recent efforts employ Transformer-based architectures to better capture long-range spectral dependencies and global context [17], [18].

Although recent methods have significantly reduced the cost of hyperspectral image acquisition, they predominantly rely on datasets focused on objects and outdoor scenes [9], [19]–[21]. In contrast, the scarcity of human-centered hyperspectral data remains largely underexplored, with only a few recent contributions such as the Hyper-Skin dataset [10]. Reconstruction models trained on conventional datasets exhibit performance degradation on human data, primarily due to the significant cross-domain distribution shifts, as demonstrated by the t-SNE plot in Fig. 1 (b).

Semi-supervised domain adaptation (SSDA) offers a promising solution for cross-domain generalization by combining fully labeled source data with a limited amount of labeled and abundant unlabeled target data. However, most existing SSDA methods are designed for classification and detection tasks [22]–[24], which differ significantly from the regression task of hyperspectral reconstruction. Even the closest SSDA studies in low-level vision tasks, such as image super-resolution [25]–[27], are not well aligned with the spectral characteristics and requirements of HSI reconstruction. Moreover, these methods typically assume a relatively sufficient amount of labeled data in the target domain, which is unrealistic in many practical scenarios, especially in medical or human-centered HSI applications [28].

Consequently, we focus on the more realistic yet challenging SSDA setting where only limited labeled target data and abundant unlabeled target data are available. As illustrated in Fig. 1 (a), a clear distribution shift exists between the fully labeled source domain (object/scene datasets such as NTIRE2022 [9]) and the sparsely labeled target domain

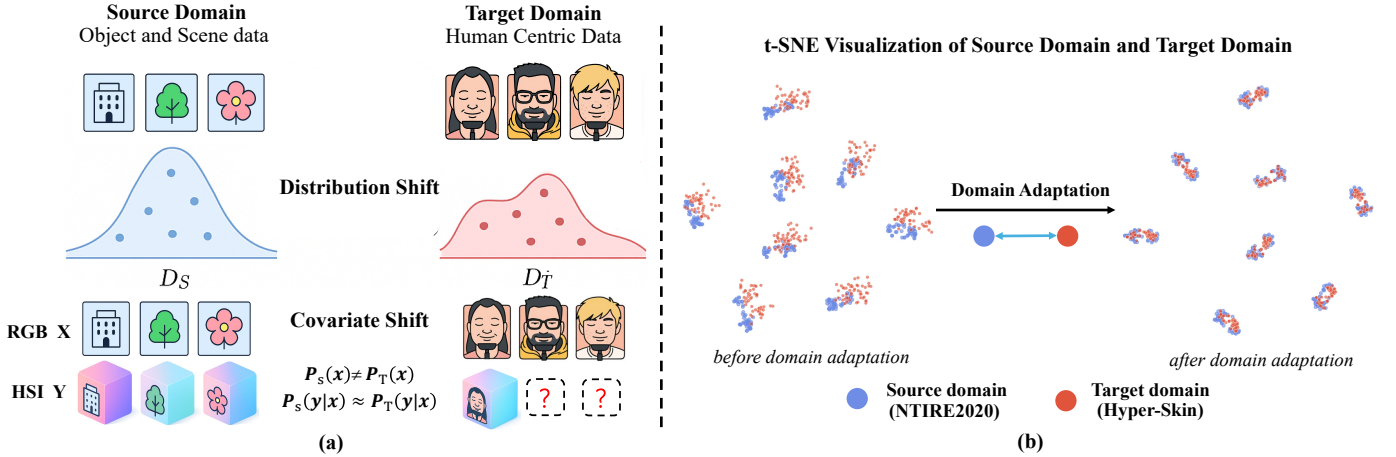


Fig. 1. Illustration of the domain adaptation scenario in HSI reconstruction under the SSDA paradigm. (a) Illustration of distribution shift between the source domain (D_S) and target domain (D_T), primarily reflecting covariate shift with similar conditional distributions. The source domain is fully labeled, while the target domain contains only a few labeled samples. (b) t-SNE visualization of features before and after adaptation. Our method aligns features across source (NTIRE2022) [9] and target (Hyper-Skin [10]) domain features using both labeled and unlabeled data.

(human-centric Hyper-Skin), primarily manifested as covariate shift ($P_S(x) \neq P_T(x)$), while the conditional distributions remain similar ($P_S(y|x) \approx P_T(y|x)$) [29]. Such a shift poses a significant challenge for hyperspectral image reconstruction, especially in human-centric scenarios where labeled data is expensive and scarce.

To this end, we propose SpectralAdapt, an SSDA method for hyperspectral image reconstruction that extracts domain-invariant spectral features under limited supervision to enable effective cross-domain adaptation. SpectralAdapt builds upon the Mean Teacher paradigm [30], which promotes consistency learning between a student and a teacher network under limited supervision [30]. To better exploit the unlabeled target data, SpectralAdapt enhances spectral reasoning through Spectral Density Masking (SDM), which encourages the student model to focus on masked regions and learn inter-channel dependencies. Given that the spectral information embedded in RGB channels varies across domains, SDM adaptively determines masking ratios using a metric derived from the Spectral Angle Mapper (SAM) [31], thereby guiding the model to recover informative content from complementary cues. To further improve spectral alignment with physical interpretability, we introduce the Spectral Endmember Representation Alignment (SERA) module. SERA extracts spectral endmembers from labeled data to construct a dynamic endmember bank that serves as domain-invariant anchors, encouraging the model to produce predictions that are both semantically consistent and physically meaningful. By incorporating this physically grounded inductive bias, SERA facilitates robust spectral alignment under limited supervision.

In summary, we tackle the challenge of limited labeled human HSI data in HSI reconstruction by proposing a novel approach, SpectralAdapt, which integrates spectral density masking SDM and endmember-guided spectral alignment SERA to improve domain generalization, spectral learning, and reconstruction fidelity. Our contributions can be summarized as follows:

- To the best of our knowledge, we are the first to apply SSDA to hyperspectral image reconstruction, enabling knowledge transfer from object-based HSI datasets to human-centered data using limited labeled and abundant unlabeled data.
- We develop a Spectral Density Masking (SDM) strategy that enhances spectral reasoning by assigning adaptive masking ratios across RGB channels based on spectral complexity, thereby improving cross-channel representation learning.
- We design a Spectral Endmember Representation Alignment (SERA) module that constructs a dynamic endmember bank from labeled data to serve as domain-invariant anchors, guiding unlabeled predictions toward physically meaningful spectra.
- Extensive experiments on both cross-domain reconstruction and downstream medical segmentation tasks demonstrate that our method consistently outperforms existing state-of-the-art SSDA approaches in low-label regimes, achieving superior spectral fidelity and strong generalization to clinical HSI applications.

II. RELATED WORK

A. Hyperspectral Image Reconstruction

Hyperspectral image (HSI) reconstruction is a fundamental task in both remote sensing and computer vision, aiming to generate high-resolution spectral data from low-dimensional or compressed inputs. HSI data contains hundreds of narrow and contiguous spectral bands, offering fine-grained material discrimination, but traditional acquisition systems are constrained by high cost and long scanning time. Recent advances in deep learning have significantly improved the accuracy and efficiency of HSI reconstruction [32]–[34]. In particular, convolutional neural networks (CNNs) and transformer-based architectures have shown strong capabilities in modeling spatial-spectral correlations, enabling end-to-end learning of spectral recovery mappings.

To improve the accessibility of HSI, many recent works have explored reconstruction from more readily available inputs. A prominent direction focuses on RGB-to-HSI reconstruction [11], [35], [36], leveraging the statistical correlations between RGB and hyperspectral representations. For example, Yan et al. [35] employ a two-stage CNN to progressively refine spectral details, while Zhang et al. [11] introduce a transformer-based network to model both local textures and global spectral dependencies.

Beyond RGB-based approaches, another important work focuses on reconstructing HSI from compressed measurements. Coded Aperture Snapshot Spectral Imaging (CASSI) systems [17], [37]–[39] encode multiplexed spectral information into a single 2D snapshot via optical modulation, enabling faster acquisition but requiring computational spectral recovery. These methods typically exploit the inherent redundancy and compressibility of HSI data [18], [40], [41], using deep priors or learned inverse mappings to reconstruct the spectral cube. For instance, Cai et al. [17] propose a masking strategy to regularize spectral recovery, while Chen et al. [37] adopt an unrolled optimization framework that mimics iterative solvers for improved convergence and interpretability.

Despite their progress, most existing HSI reconstruction models are trained and evaluated within a single-domain setting, often limited to specific sensors or acquisition environments. When deployed across different imaging systems, lighting conditions, or object categories, these models typically suffer significant performance degradation due to domain shifts. This generalization gap has motivated growing interest in domain adaptation and generalization techniques. Incorporating such strategies into the HSI reconstruction pipeline is essential for building deployable models across diverse real-world scenarios.

B. Semi-Supervised Domain Adaptation

Semi-supervised domain adaptation (SSDA) has been widely adopted to tackle domain shift and label scarcity in various vision tasks, particularly image classification and semantic segmentation [42], [43]. Existing SSDA methods can be broadly categorized into three paradigms: (i) consistency-regularized pseudo-labeling, (ii) mixup-based interpolation, and (iii) prototype-driven domain alignment.

Consistency-regularized pseudo-labeling methods aim to generate pseudo-labels for unlabeled target samples and enforce prediction consistency under various perturbations [44]. Representative approaches include ADA-SDA [45], which employs adaptive confidence thresholds for pseudo-label selection, and MCL-SDA [46], which introduces multi-view consistency regularization across different classifiers. While effective in classification, these methods struggle in hyperspectral reconstruction due to the continuous, high-dimensional output space, which makes pseudo-labels inherently unstable and consistency objectives difficult to enforce.

Mixup-based methods seek to reduce domain discrepancy by constructing synthetic samples via interpolation between source and target instances [47]. IDM-SDA [48] performs inter-domain mixup at the input level to bridge the feature

gap, while SFPM-SDA [49] progressively mixes labeled and pseudo-labeled samples to stabilize training. However, applying mixup to hyperspectral data can lead to physically implausible spectra and blurry reconstructions, compromising spectral fidelity.

Prototype-based alignment strategies, such as PRO-SDA [50] and Unmix-SDA [51], focus on aligning distributions by leveraging representative prototypes. PRO-SDA learns class-agnostic prototypes to guide alignment, whereas Unmix-SDA introduces spectral unmixing to derive representative endmembers for each domain. These methods, however, are less effective for HSI reconstruction, where discrete prototypes are ill-defined and reliable endmember estimation is challenging due to cross-domain variability.

Overall, most existing SSDA methods are designed for classification or segmentation tasks and assume discrete label spaces, making them ill-suited for hyperspectral reconstruction—a dense, continuous regression problem with strict spectral fidelity requirements. To address these limitations, we propose a new SSDA framework tailored for HSI reconstruction. Our approach integrates spectral priors through spectral density masking and introduces endmember-guided alignment to enhance spectral consistency and domain generalization.

III. PRELIMINARY DEFINITIONS

Given a standard RGB image $x \in \mathbb{R}^{H \times W \times 3}$, the goal of hyperspectral image (HSI) reconstruction is to predict its high-dimensional hyperspectral counterpart $y \in \mathbb{R}^{H \times W \times C}$, where C denotes the number of spectral bands. In the semi-supervised domain adaptation (SSDA) setting, we consider two domains: a general-domain source dataset $\mathcal{D}_l^S = \{(x_i^S, y_i^S)\}_{i=1}^{L_S}$ with full supervision, and a human-centered target dataset that includes a small labeled subset $\mathcal{D}_l^T = \{(x_i^T, y_i^T)\}_{i=1}^{L_T}$ and a large unlabeled subset $\mathcal{D}_u^T = \{x_i^T\}_{i=1}^{U_T}$, where $L_T \ll L_S$ and $L_T \ll U_T$. The goal is to learn a reconstruction function f_θ that achieves accurate HSI reconstruction on the unlabeled target samples by effectively leveraging labeled source data and a limited amount of labeled target data.

To address the domain gap between the source and target domains, we design two complementary modules at different levels of learning process. At the input level, the Spectral Density Masking (SDM) module selectively perturbs spectrally complex RGB regions to reduce covariate shift and encourage learning from transferable cues. At the representation level, the Spectral Endmember Representation Alignment (SERA) module aligns the predicted hyperspectral features with a shared spectral basis, constructed from labeled pixels in both domains. These domain-invariant anchors impose physically grounded constraints and guide the model to learn consistent spectral representations across domains.

Our overall objective is to reduce the discrepancy between the feature distributions of the source and target domains. Let $p(f_\theta(x^S))$ and $p(f_\theta(x^T))$ denote the feature distributions induced by the reconstruction model f_θ on the source and

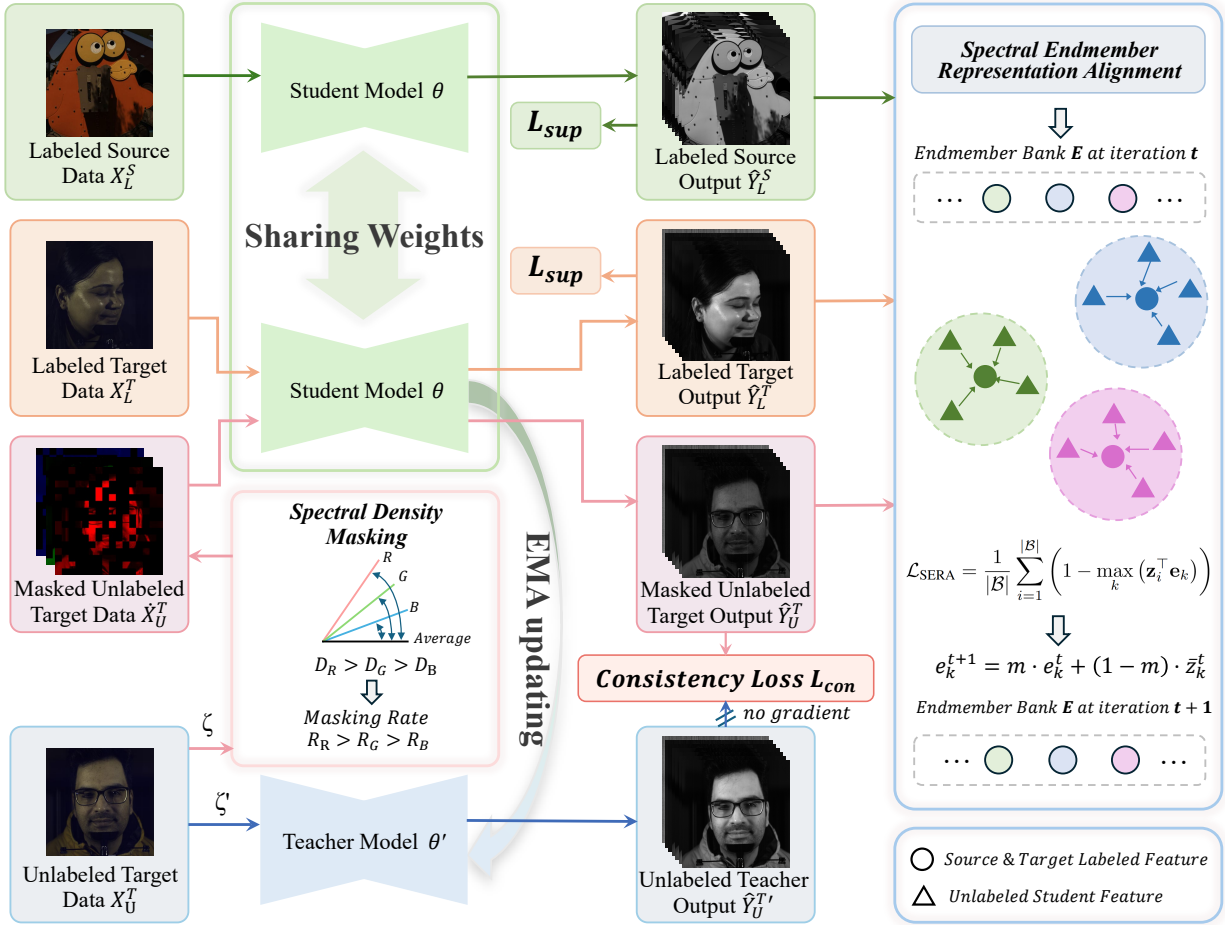


Fig. 2. Overview of our proposed method. ζ (weak) and ζ' (strong) denote two stochastic augmentations applied to the same input before the student and teacher, θ, θ' represents student and teacher model parameters respectively, where student and teacher model share the same architecture and θ' is updated through the Exponential Moving Average (EMA) of θ . Spectral density masking (SDM) adaptively masks RGB regions based on spectral complexity to enhance spectral reasoning, and the spectral endmember representation alignment (SERA) aligns predictions with physically meaningful endmembers to improve domain transferability.

target inputs, respectively. We formalize the domain alignment objective as:

$$\mathcal{L}_{align} = D(p(f_\theta(x^S)), p(f_{\theta'}(x^T))), \quad (1)$$

where $D(\cdot, \cdot)$ denotes distributional distance metric. Reducing this discrepancy encourages the model to learn domain-invariant spectral representations, thereby improving generalization to the unlabeled target domain.

IV. METHODOLOGY

A. Network Overview

We propose a novel semi-supervised domain adaptation (SSDA) method for hyperspectral image reconstruction, built upon the Mean Teacher paradigm [30], as illustrated in Fig. 2. The model comprises a student-teacher model pair, where the student is optimized via supervised learning, and the teacher is updated through the exponential moving average (EMA) of the student's parameters. For labeled samples from both the source domain \mathcal{D}_l^S and the target domain \mathcal{D}_l^T , we apply a supervised reconstruction loss \mathcal{L}_{sup} to minimize the discrepancy between predicted and ground-truth hyperspectral images. For

unlabeled target data \mathcal{D}_u^T , we adopt dual-view augmentation: distinct transformations are applied to the same input before feeding it into the student and teacher networks, respectively. To handle the spectral imbalance in RGB-based inputs, we integrate a Spectral Density Masking (SDM) strategy, which assigns adaptive masking ratios to each RGB channel based on its estimated spectral complexity, thereby preserving more informative spectral regions. The student model is trained to match the teacher's predictions on augmented views through a consistency loss \mathcal{L}_{con} . Moreover, we introduce a Spectral Endmember Representation Alignment (SERA) loss \mathcal{L}_{SERA} , which encourages the predicted hyperspectral features to align with a dynamic bank of physically interpretable endmembers extracted from labeled data. This alignment serves as a spectral inductive bias, improving domain transferability and representation consistency.

B. Spectral Density Masking (SDM)

The masking-based learning mechanism has proven effective within the Mean Teacher framework [30], as it enhances the model's ability to attend to semantically meaningful re-

regions, thereby improving both image understanding and representation learning [52]–[54]. However, most reconstruction models treat the three RGB channels uniformly, implicitly assuming a uniform distribution of spectral information. Nevertheless, this assumption does not hold in practice—information density varies significantly across different wavelengths. For example, in the case of human face skin shown in Fig. 3, the blue–green spectral regions (450–490 nm and 520–580 nm) typically exhibit smooth and predictable reflectance profiles, which makes them relatively easier to approximate. In contrast, the red spectral region (600–700 nm) demonstrates more pronounced variations in reflectance, suggesting a higher concentration of discriminative information and increased spectral complexity.

To address spectral imbalance across different wavelength regions, we propose Spectral Density Masking (SDM), a strategy that adaptively adjusts the masking ratio based on the spectral complexity of each region. Specifically, we quantify the importance of a spectral region by evaluating the change in spectral consistency when replacing it with its spatial average.

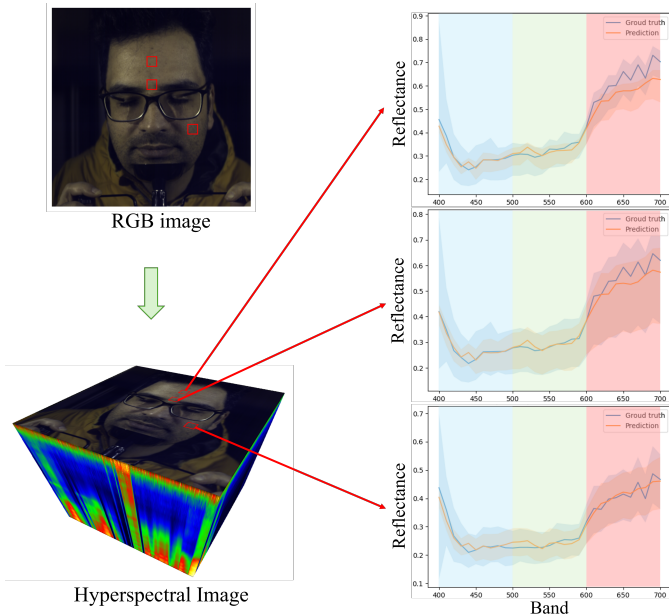


Fig. 3. **Spectral Density Masking Illustration.** We visualize three sampled regions from an RGB image (top left) and their corresponding reflectance spectra from the ground truth hyperspectral image (bottom left). The spectral bands are across the 400–700 nm range and color-coded into blue (400–500 nm), green (510–580 nm), and red (600–700 nm). Notably, higher angular deviations in the red region indicate greater spectral complexity, which motivates our Spectral Density Masking (SDM) strategy.

Given a hyperspectral image cube $\mathbf{X} \in \mathbb{R}^{H \times W \times C}$, where C denotes the number of spectral channels, we reshape it into a two-dimensional spectral matrix $\mathbf{S} \in \mathbb{R}^{N \times C}$, where $N = H \cdot W$, such that each row represents the spectral vector of a single pixel. For a spectral region $b \in \{\text{B}, \text{G}, \text{R}\}$ with associated channel indices $I_b \subseteq \{1, \dots, C\}$, we construct a perturbed spectrum $\mathbf{S}^{(b)}$ by replacing the channels in I_b with the global spatial average across all pixels:

$$\mathbf{S}_{n,c}^{(b)} = \begin{cases} \bar{S}_c, & \text{if } c \in I_b, \\ \mathbf{S}_{n,c}, & \text{otherwise,} \end{cases} \quad \text{for } n = 1, \dots, N, \quad (2)$$

where \bar{S}_c denotes the global average of each spectral channel and is defined as:

$$\bar{S}_c = \frac{1}{N} \sum_{n=1}^N \mathbf{S}_{n,c}. \quad (3)$$

To assess the contribution of region b to the overall spectral information, we compute the spectral deviation between the original and perturbed spectra using the Spectral Angle Mapper (SAM) [31]. Given two spectral matrices $\mathbf{A}, \mathbf{B} \in \mathbb{R}^{N \times C}$, the SAM is defined as:

$$\text{SAM}(\mathbf{A}, \mathbf{B}) = \frac{1}{N} \sum_{n=1}^N \arccos \left(\frac{\langle \mathbf{A}_n, \mathbf{B}_n \rangle}{\|\mathbf{A}_n\|_2 \cdot \|\mathbf{B}_n\|_2 + \varepsilon} \right), \quad (4)$$

where \mathbf{A}_n and \mathbf{B}_n denote the spectral vectors of the n -th pixel, $\langle \cdot, \cdot \rangle$ denotes the dot product, $\|\cdot\|_2$ is the ℓ_2 norm, and ε is a small constant to prevent numerical instability. Finally, we define the spectral density \mathcal{D} of region b as the SAM between the original and perturbed spectra:

$$\mathcal{D}_b = \text{SAM}(\mathbf{S}^{(b)}, \mathbf{S}). \quad (5)$$

A higher value of \mathcal{D}_b indicates that region b contributes more significantly to the spectral representation and is thus masked more aggressively during training. This targeted masking compels the model to exploit informative cues from lower-density regions, promoting a more comprehensive understanding of high-density spectral features and cross-channel dependencies. Based on the computed spectral density \mathcal{D}_b for each region $b \in \{\text{R}, \text{G}, \text{B}\}$, we derive adaptive masking ratios $\mathbf{r} = [r_{\text{R}}, r_{\text{G}}, r_{\text{B}}]$ using min-max normalization:

$$r_b = r_{\min} + \frac{\mathcal{D}_b - \min(\mathcal{D})}{\max(\mathcal{D}) - \min(\mathcal{D})} \cdot (r_{\max} - r_{\min}), \quad (6)$$

where r_{\min} and r_{\max} are predefined lower and upper bounds, and $\mathcal{D} = [\mathcal{D}_{\text{R}}, \mathcal{D}_{\text{G}}, \mathcal{D}_{\text{B}}]$. We then apply channel-wise block masking based on the computed ratios. For each RGB channel, a fraction r_b of spatial blocks (of size $s \times s$) is randomly selected and masked out. The binary block mask is upsampled to the original resolution and applied element-wise to the corresponding channel. This strategy promotes selective information masking, where spectrally dominant regions are masked more aggressively to encourage the model to extract complementary features from less informative areas and enhance its spectral modeling capacity.

C. Spectral Endmember Representation Alignment (SERA)

In hyperspectral image (HSI) analysis, spectral endmembers are pure spectral signatures essential for unmixing pixels with mixed spectra [55]. In deep learning, analogous endmembers serve as representative feature vectors that anchor the embedding space, enhancing interpretability and domain transferability. This is particularly valuable in domain adaptation with

limited labeled target data. By initializing the representative vectors with physically meaningful endmembers, we introduce an inductive bias that guides the model to learn spectrum-constrained features that are discriminative and domain-robust.

To construct the endmember bank, we randomly sample individual pixel spectra from labeled source HSI Y_L^S and labeled target HSI Y_L^T . Each sampled pixel corresponds to a spectral vector of dimension C , and the resulting matrix $\mathbf{S} \in \mathbb{R}^{N \times C}$ is formed by stacking N such vectors as rows. All spectral vectors are individually normalized to unit ℓ_2 -norm to ensure scale invariance. We adopt the Automated Target Generation Process (ATGP) [56] to greedily select K representative endmembers from \mathbf{S} by maximizing orthogonal projection residuals, thereby ensuring spectral diversity. The first endmember \mathbf{e}_1 is chosen as the spectral vector with the maximum ℓ_2 -norm:

$$\mathbf{e}_1 = \arg \max_{\mathbf{s}_n \in \mathbf{S}} \|\mathbf{s}_n\|_2. \quad (7)$$

For each subsequent step $k = 2, \dots, K$, let $\mathbf{E}_{k-1} = [\mathbf{e}_1, \dots, \mathbf{e}_{k-1}] \in \mathbb{R}^{C \times (k-1)}$ be the matrix of already selected endmembers. The k -th endmember \mathbf{e}_k is selected as the spectral vector with the largest projection residual relative to the subspace spanned by \mathbf{E}_{k-1} :

$$\mathbf{e}_k = \arg \max_{\mathbf{s}_n \in \mathbf{S}} \|(\mathbf{I} - \mathbf{P}_{k-1}) \mathbf{s}_n\|_2, \quad (8)$$

where the projection matrix \mathbf{P}_{k-1} is defined as:

$$\mathbf{P}_{k-1} = \mathbf{E}_{k-1} (\mathbf{E}_{k-1}^\top \mathbf{E}_{k-1})^{-1} \mathbf{E}_{k-1}^\top. \quad (9)$$

Intuitively, ATGP iteratively selects pixels that are maximally spectrally distinct from the subspace spanned by the previously chosen endmembers. After K iterations, the final endmembers are denoted as:

$$\mathbf{ATGP}(\mathbf{S}, K) = [\mathbf{e}_1, \dots, \mathbf{e}_K]^\top \in \mathbb{R}^{K \times C}. \quad (10)$$

Each endmember \mathbf{e}_k is then normalized to lie on the unit hypersphere, forming the initial spectral endmember bank \mathbf{E}^0 :

$$\mathbf{E}^0 = \text{Norm}(\mathbf{ATGP}(\mathbf{S}, K)) \in \mathbb{R}^{K \times C}, \quad (11)$$

which serves as a physically grounded anchor for feature alignment during contrastive training.

During training, the reconstruction model generates hyperspectral predictions from labeled source data $\hat{\mathbf{Y}}_l^S$, labeled target data $\hat{\mathbf{Y}}_l^T$, and unlabeled target inputs, yielding predicted outputs $\hat{\mathbf{Y}}_u^T \in \mathbb{R}^{H \times W \times C}$. To obtain a compact and discriminative spectral representation, each predicted hyperspectral output $\hat{\mathbf{Y}}$ is processed via global average pooling across the spatial dimensions, followed by ℓ_2 -normalization:

$$\mathbf{z} = \text{Norm}(\text{AvgPool}(\hat{\mathbf{Y}})), \quad \text{Norm}(\mathbf{z}) = \frac{\mathbf{z}}{\|\mathbf{z}\|_2}. \quad (12)$$

This transformation yields a unit-norm feature vector $\mathbf{z} \in \mathbb{R}^C$, which encapsulates the global spectral characteristics of the reconstructed output. For each spectral feature \mathbf{z}_i in a mini-batch $\mathcal{B} = \{\mathbf{z}_i\}_{i=1}^{|\mathcal{B}|}$, the most relevant endmember is identified by selecting the one with the highest cosine similarity, i.e., the

largest inner product $\mathbf{z}_i^\top \mathbf{e}_k$, from the endmember bank. The spectral endmember alignment loss $\mathcal{L}_{\text{SERA}}$ is then defined as:

$$\mathcal{L}_{\text{SERA}} = \frac{1}{|\mathcal{B}|} \sum_{i=1}^{|\mathcal{B}|} \left(1 - \max_k (\mathbf{z}_i^\top \mathbf{e}_k) \right), \quad (13)$$

which encourages each predicted spectral feature to remain closely aligned with its most semantically or physically relevant endmember, thereby enhancing the discriminability and domain generalizability of the learned representations.

To enable the endmember bank to evolve alongside the model while maintaining the interpretability of its initial structure, we adopt a momentum-based update strategy. Specifically, at iteration t , each endmember \mathbf{e}_k^t is updated as:

$$\bar{\mathbf{z}}_k^t = \frac{1}{|\mathcal{B}_k^t|} \sum_{i \in \mathcal{B}_k^t} \mathbf{z}_i^t, \quad (14)$$

$$\mathbf{e}_k^t = \text{Norm} (m \cdot \mathbf{e}_k^{t-1} + (1 - m) \cdot \bar{\mathbf{z}}_k^t), \quad (15)$$

where $a_i = \arg \max_j (\mathbf{z}_i^{t-1} \mathbf{e}_j^{t-1})$ assigns each feature \mathbf{z}_i^t to its most similar endmember from the previous iteration, and $\mathcal{B}_k^t = \{i \mid a_i = k\}$ denotes the set of features currently assigned to endmember k . The momentum coefficient m controls the update rate. This update scheme allows the endmembers to gradually adapt to the evolving feature distribution without compromising their original physical semantics.

D. Objective Function

The overall training objective is to minimize a total loss $\mathcal{L}_{\text{total}}$, which consists of a supervised component \mathcal{L}_{sup} and an unsupervised component \mathcal{L}_{un} , formulated as:

$$\mathcal{L}_{\text{total}} = \mathcal{L}_{\text{sup}}^{\text{total}} + \mathcal{L}_{\text{un}}^{\text{total}}. \quad (16)$$

1) *Supervised Loss \mathcal{L}_{sup}* : The supervised loss \mathcal{L}_{sup} is defined as a weighted sum of the pixel-wise \mathcal{L}_1 loss and the Structural Similarity Index Measure (SSIM) loss $\mathcal{L}_{\text{SSIM}}$ [57]. The \mathcal{L}_1 loss ensures precise reconstruction at pixel level, while $\mathcal{L}_{\text{SSIM}}$ encourages structural fidelity and perceptual quality. Given predicted output \hat{y} and ground truth y , the two components are formulated as:

$$\mathcal{L}_1(\hat{y}, y) = \frac{1}{N} \sum_{i=1}^N |\hat{y}_i - y_i|, \quad (17)$$

$$\mathcal{L}_{\text{SSIM}}(\hat{y}, y) = 1 - \text{SSIM}(\hat{y}, y), \quad (18)$$

$$\text{SSIM}(\hat{y}, y) = \frac{(2\mu_{\hat{y}}\mu_y + C_1)(2\sigma_{\hat{y}y} + C_2)}{(\mu_{\hat{y}}^2 + \mu_y^2 + C_1)(\sigma_{\hat{y}}^2 + \sigma_y^2 + C_2)}, \quad (19)$$

where $\mu_{\hat{y}}, \mu_y$ are the mean values, $\sigma_{\hat{y}}^2, \sigma_y^2$ are variances, and $\sigma_{\hat{y}y}$ is the covariance. Constants $C_1 = (K_1 L)^2$ and $C_2 = (K_2 L)^2$ are stabilization terms, where L is the dynamic range of pixel values, with $K_1 = 0.01$ and $K_2 = 0.03$. For labeled data from both source and target domains, the supervised loss is defined as:

$$\mathcal{L}_{\text{sup}}(\hat{y}, y) = \lambda_{\text{sup}} \cdot \mathcal{L}_1(\hat{y}, y) + (1 - \lambda_{\text{sup}}) \cdot \mathcal{L}_{\text{SSIM}}(\hat{y}, y), \quad (20)$$

where $\lambda_{\text{sup}} \in [0, 1]$ balances pixel accuracy and structural consistency.

Given predictions and ground truths (\hat{y}_L^S, y_L^S) from the labeled source domain and (\hat{y}_L^T, y_L^T) from the labeled target domain, the total supervised loss becomes:

$$\mathcal{L}_{\text{sup}}^{\text{total}} = \mathcal{L}_{\text{sup}}(\hat{y}_L^S, y_L^S) + \mathcal{L}_{\text{sup}}(\hat{y}_L^T, y_L^T). \quad (21)$$

2) *Unsupervised Loss \mathcal{L}_{un}* : To leverage unlabeled target data in the semi-supervised domain adaptation setting, the unsupervised loss \mathcal{L}_{un} enforces both prediction consistency and spectral structure alignment.

Given an unlabeled input x_U , we apply two different augmentations to generate student and teacher predictions \hat{y}_U^T and $\hat{y}_U^{T'}$, respectively. The consistency loss is then defined as:

$$\mathcal{L}_{\text{con}}(\hat{y}_U^T, \hat{y}_U^{T'}) = \mathcal{L}_1(\hat{y}_U^T, \hat{y}_U^{T'}), \quad (22)$$

To further enforce spectral structure alignment, we introduce the spectral endmember regularization loss $\mathcal{L}_{\text{SERA}}$, as described in Section IV-C, which guides predicted spectra toward physically meaningful endmembers. Overall, the total unsupervised loss is formulated as:

$$\mathcal{L}_{\text{un}}^{\text{total}} = \lambda_{\text{un}} \cdot \mathcal{L}_{\text{con}} + (1 - \lambda_{\text{un}}) \cdot \mathcal{L}_{\text{SERA}}, \quad (23)$$

where $\lambda_{\text{un}} \in [0, 1]$ controls the trade-off between consistency regularization and endmember-based alignment.

V. EXPERIMENT

A. Task Overview

We conduct a two-stage evaluation to comprehensively assess both the transferability and downstream utility of the proposed method. (1) We evaluate the semi-supervised domain adaptation (SSDA) capability of our model by transferring knowledge from a large-scale object-centric dataset (NTIRE [9], [58]) to a human-centric dataset (Hyper-Skin [10]), which presents a significant domain shift. (2) We assess the utility of the reconstructed hyperspectral images (RS-HSI) for downstream tasks. Specifically, we perform pixel-wise semantic segmentation on two human medical benchmarks: Choledoch and HeiPorSPECTRAL datasets. The evaluation includes three input modalities—RGB, raw HSI, and RS-HSI—with all settings using the same segmentation backbone to ensure fair comparison across modalities.

B. Experiment Datasets

1) *Source Domain: NTIRE 2020 and NTIRE 2022 Datasets*. We use the NTIRE 2020 and NTIRE 2022 datasets as the source domain in our domain adaptation experiments. These datasets were released as part of the NTIRE Spectral Reconstruction Challenges [9], [58], and contain hyperspectral images (HSI) of diverse objects and scenes collected with a Specim IQ push-broom camera at native resolution $512 \times 512 \text{px}$ and 204 spectral bands (400–1000 nm), then resampled to 31 VIS bands (10 nm spacing) for the challenge. NTIRE 2020 includes 460 images, while NTIRE 2022 includes 1,000 images. All images are resampled to 31 spectral bands spanning the 400–700 nm visible range.

2) *Target Domain: Hyper-Skin Dataset*. The Hyper-Skin dataset [10], introduced in the NeurIPS 2023 Hyper-Skin Challenge, serves as the target domain for domain adaptation. It comprises 330 hyperspectral facial images collected from 51 human participants, with spectral coverage from 400 to 700 nm across 31 bands at a spatial resolution of 1024. This spectral range corresponds to the visible spectrum, enabling fair comparison with RGB-based reconstruction methods. All data collection procedures were approved by the relevant Institutional Review Board (IRB), and written informed consent was obtained from all participants.

3) *Downstream Evaluation Datasets: Multidimensional Choledoch Dataset*. The Multidimensional Choledoch Dataset [59] is a pathology benchmark used to assess the downstream utility of reconstructed HSI. It consists of 880 microscopy scenes from 174 patients, with paired RGB and hyperspectral images captured across 60 bands in the 550–1000 nm range using an AOTF-based imaging system. We extract 31 bands to ensure consistency with the source domain. Expert-annotated XML polygon masks are provided to identify cancer regions, including both partially and fully cancerous samples, enabling quantitative evaluation of HSI-driven segmentation.

HeiPorSPECTRAL Dataset. The HeiPorSPECTRAL dataset [60] is the only publicly available hyperspectral imaging (HSI) dataset covering a comprehensive set of internal organs. It contains high-resolution images of 20 physiological porcine organs collected from 11 pigs, with 8 pigs recorded per organ. Each image captures a 480×640 scene across 100 spectral bands ranging from 500–1000 nm, acquired using the medically certified TIVITA Tissue system. To ensure domain consistency, we uniformly subsample 31 spectral bands from the original datacube. Expert-annotated polygon masks delineate physiologically representative tissue regions while avoiding confounding artifacts such as deformation, blood stains, or perfusion defects. Due to the anatomical and spectral similarity between porcine and human organs, HeiPorSPECTRAL serves as a valuable surrogate for human-organ-related validation in clinical HSI research.

C. Experimental Settings

Experimental Environment. All experiments in our work are implemented in PyTorch 1.12.1 and conducted under Python 3.7.16 running on an NVIDIA A40 GPU.

Reconstruction Model Backbone. In our experiments, we adopt MST++ [61], the winner of NTIRE 2022 spectral recovery challenge, as the backbone for all experiments.

Training details. The network was trained using the Adam optimizer for 1000 iterations with an initial learning rate of 1×10^{-4} , which was updated using a decaying learning rate schedule. The batch sizes for source domain and unlabeled target domain data were set to 8, and the batch size for labeled target data was 1. We set the momentum for the EMA-based teacher model to $m_{\text{ema}} = 0.99$, and the momentum for updating the endmember bank to $m_{\text{end}} = 0.9$. The total loss combines supervised and unsupervised terms with weights $\lambda_{\text{sup}} = 0.4$ and $\lambda_{\text{un}} = 0.3$, respectively. Based on ablation

TABLE I

STATISTICAL COMPARISON OF OUR PROPOSED METHOD WITH OTHER SSDA METHODS, USING NTIRE2020 OR NTIRE2022 AS SOURCE DOMAIN AND HYPER-SKIN AS TARGET DOMAIN. SSIM, SAM, AND PSNR INDICATE STRUCTURAL SIMILARITY INDEX, SPECTRAL ANGLE MAPPER, AND PEAK SIGNAL-TO-NOISE RATIO, RESPECTIVELY. ‘SOURCE-ONLY’ REFERS TO A MODEL PRE-TRAINED ONLY ON THE SOURCE DATASET, WHILE ‘FULLY-SUPERVISED’ INVOLVES TRAINING MODEL WITH FULLY LABELED TARGET DATA. ‘BASELINE’ REPRESENTS THE STANDARD SSDA MODEL USING THE MEAN TEACHER FRAMEWORK, AND ‘LABELED’ INDICATES THE NUMBER OF LABELED SAMPLES IN THE TARGET DATASET.

Method	Labeled (Ratio[%])	NTIRE2020 → Hyper-Skin			NTIRE2022 → Hyper-Skin		
		SSIM (% , \uparrow)	SAM (% , \downarrow)	PSNR (\uparrow)	SSIM (% , \uparrow)	SAM (% , \downarrow)	PSNR (\uparrow)
Source-Only	0 (0%)	59.87 \pm 8.31	67.57 \pm 6.52	17.86 \pm 1.29	59.87 \pm 8.31	67.57 \pm 6.52	17.86 \pm 1.29
Fully-Supervised	N (100%)	94.53 \pm 5.07	14.00 \pm 2.39	31.12 \pm 2.54	94.53 \pm 5.07	14.00 \pm 2.39	31.12 \pm 2.54
ADA-SDA [45]	1 (0.5%)	80.37 \pm 8.57	21.47 \pm 3.79	20.09 \pm 1.45	81.30 \pm 7.33	23.31 \pm 1.72	25.44 \pm 1.37
SFPM-SDA [49]		81.92 \pm 6.87	20.21 \pm 3.09	19.67 \pm 1.42	81.55 \pm 8.93	23.90 \pm 1.46	22.55 \pm 1.67
MCL-SDA [46]		82.31 \pm 9.10	22.61 \pm 1.74	21.23 \pm 1.92	82.72 \pm 9.01	25.79 \pm 1.31	20.71 \pm 1.56
IDM-SDA [48]		83.33 \pm 9.38	20.76 \pm 1.76	22.82\pm1.98	83.70 \pm 9.36	21.67 \pm 1.67	21.95 \pm 2.20
Unmix-SDA [51]		83.42 \pm 9.98	22.45 \pm 1.57	22.78 \pm 1.89	84.05 \pm 9.11	20.32 \pm 2.02	25.74 \pm 2.08
PRO-SDA [50]		83.07 \pm 10.21	23.62 \pm 1.61	22.31 \pm 2.05	84.26 \pm 8.85	21.23 \pm 2.08	24.63 \pm 2.03
Baseline [30]	1 (0.5%)	79.98 \pm 8.24	27.51 \pm 2.70	20.17 \pm 1.53	80.74 \pm 8.60	21.72 \pm 1.88	20.71 \pm 1.52
SpectralAdapt (Ours)		84.37\pm8.06	19.32\pm1.45	22.04 \pm 1.93	85.70\pm7.78	18.62\pm1.95	28.13\pm1.79
ADA-SDA [45]	3 (1.5%)	86.16 \pm 8.89	18.40 \pm 1.80	24.23 \pm 2.25	86.49 \pm 9.09	19.11 \pm 3.09	26.20 \pm 1.93
SFPM-SDA [49]		85.69 \pm 8.91	21.87 \pm 1.50	23.75 \pm 1.86	87.05 \pm 9.73	18.95 \pm 2.34	27.82 \pm 2.66
MCL-SDA [46]		86.60 \pm 8.88	18.90 \pm 1.73	25.20 \pm 1.43	86.92 \pm 9.35	19.21 \pm 2.26	24.78 \pm 2.75
IDM-SDA [48]		87.35 \pm 9.98	14.97 \pm 3.17	26.15 \pm 2.71	88.36 \pm 9.88	14.88 \pm 3.50	30.08 \pm 3.14
Unmix-SDA [51]		87.82 \pm 9.66	15.73 \pm 3.18	27.25 \pm 2.17	88.41 \pm 10.09	18.32 \pm 2.41	29.18 \pm 2.74
PRO-SDA [50]		89.23 \pm 8.39	16.14 \pm 3.07	28.22 \pm 2.10	89.35 \pm 8.19	18.12 \pm 2.17	28.95 \pm 2.18
Baseline [30]	3 (1.5%)	85.30 \pm 9.69	23.05 \pm 2.82	23.23 \pm 1.57	85.65 \pm 7.96	25.10 \pm 2.10	27.95 \pm 2.29
SpectralAdapt (Ours)		90.24\pm7.72	17.11\pm4.56	28.78\pm2.07	91.55\pm7.16	17.76\pm2.07	30.72\pm2.06

studies V-F, we set $\lambda_{\text{sup}} = 0.4$ and $\lambda_{\text{un}} = 0.3$ to balance reconstruction accuracy and domain adaptation. To mitigate overfitting and extract more information from unlabeled data, we employed weak-strong noise augmentations (ζ), along with random flipping and random rotation. The input to the network consisted of randomly cropped 256×256 sub-volumes with a stride of 128, and a sliding window strategy was used to obtain the final prediction results.

Evaluation Metrics. To comprehensively evaluate the effectiveness of our proposed method, we conduct quantitative assessments on both the hyperspectral image reconstruction and semantic segmentation tasks. For reconstruction, we adopt three widely used metrics: Structural Similarity Index (SSIM) [57], Spectral Angle Mapper (SAM) [31], and Peak Signal-to-Noise Ratio (PSNR) [62], which jointly assess structural fidelity, spectral accuracy, and overall image quality. For the segmentation task, we employ Pixel Accuracy (PA), Mean Pixel Accuracy (MPA), and Mean Intersection over Union (mIoU) to measure classification performance at both the pixel and class levels [63], [64].

D. Comparison Experiments

As our proposed SpectralAdapt is the first semi-supervised domain adaptation (SSDA) method specifically designed for hyperspectral image reconstruction, we compare it with several state-of-the-art SSDA approaches originally developed for classification tasks, including ADA-SDA [45], IDM-SDA [48], SFPM-SDA [49], MCL-SDA [46], Unmix-SDA [51], and PRO-SDA [50]. To ensure fair comparison, we adapt each method to the reconstruction setting: ADA-SDA is adjusted to support continuous spectral outputs via regression-based pseudo-labeling and consistency losses; IDM-SDA and SFPM-SDA are adjusted to perform inter-domain and progressive

mixup in the spectral domain; MCL-SDA replaces classification heads with regression branches and enforces multi-view consistency on spectral predictions; Unmix-SDA aligns domains through spectral unmixing in a regression context; and PRO-SDA defines prototypes as representative spectral signatures rather than class centroids. To ensure a comprehensive and principled evaluation, these six baselines are selected to represent the three predominant paradigms in semi-supervised domain adaptation: pseudo-label consistency (ADA-SDA, MCL-SDA), mixup-based interpolation (IDM-SDA, SFPM-SDA), and prototype-driven alignment (Unmix-SDA, PRO-SDA).

Results on NTIRE2020 and NTIRE2022 datasets. The quantitative results of these comparative experiments are presented in Table I, showcasing the performance of domain adaptation from the NTIRE2020 and NTIRE2022 datasets to the human hyperspectral dataset, Hyper-Skin. As shown in Table I, our method consistently outperforms existing SSDA techniques across various metrics. This superior performance can be attributed to the effectiveness of our spectral prior-guided design, which explicitly models spectral characteristics and leverages physically meaningful representations. By incorporating Spectral Density Masking (SDM) and Spectral End-member Representation Alignment (SERA), our framework can effectively bridge the domain gap between general and human-centered hyperspectral data.

Unlike traditional SSDA approaches that treat all spectral channels uniformly, our method incorporates spectral density masking, which assigns adaptive masking ratios to different RGB channels based on their spectral complexity. This allows the network to better preserve and learn from information-rich spectral regions during training. Moreover, by utilizing a dynamically updated spectral endmember bank for feature

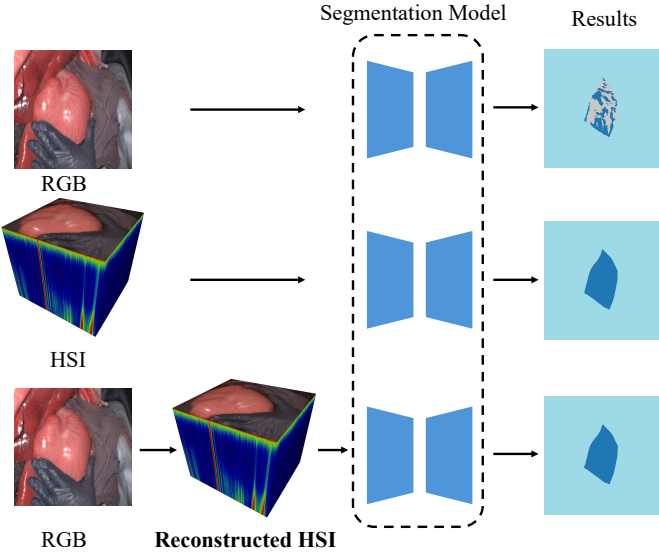


Fig. 4. Visualization of the downstream evaluation pipeline, which comprises three branches: RGB-based segmentation, HSI-based segmentation, and segmentation based on reconstructed HSI from RGB inputs. All branches utilize a shared segmentation backbone and generate pixel-wise predictions.

alignment, the model encourages consistency between predicted hyperspectral representations and physically grounded spectral structures. By combining these strategies, our method is capable of capturing key spectral patterns and domain-specific variations more effectively. As a result, our method achieves the highest SSIM, SAM, and PSNR scores on both the NTIRE2020 and NTIRE2022 datasets.

Additionally, at same label ratio, our SpectralAdapt method demonstrates significant improvements over the baseline Mean Teacher method, confirming the effectiveness of integrating spectral-aware masking and endmember-guided alignment. Remarkably, with only 3 labeled samples (1.5%), our approach nearly matches the performance of fully supervised methods, underscoring its strength and generalizability in the challenging SSDA hyperspectral image reconstruction task.

E. Downstream Validation

Downstream Evaluation Pipeline. To assess the practical utility of the reconstructed hyperspectral images (HSI), we conduct semantic segmentation experiments on two medical benchmarks: the Multidimensional Choledoch and HeiPorSPECTRAL datasets. As illustrated in Fig.4, we compare three input modalities: RGB images, raw HSI, and HSI reconstructed from RGB. For a fair comparison, all inputs are fed into the same segmentation architecture under identical training and evaluation protocols. Specifically, we adopt a standard UNet [65] as the segmentation backbone and only adjust the first convolutional layer to accommodate the input dimensionality of each modality.

Reconstructing HSI from RGB. We apply several SSDA methods, including our proposed SpectralAdapt, to reconstruct hyperspectral representations from RGB under the standard 10% label setting [66], [67]. As shown in Table II, SpectralAdapt consistently achieves superior SSIM and PSNR on both

TABLE II
RECONSTRUCTION PERFORMANCE (%) OF RECENT SSDA METHODS ON MEDICAL HYPERSPECTRAL DATASETS. SSIM AND PSNR ARE REPORTED ON CHOLEDOCH AND HEIPORSPECTRAL USING 10% LABELED DATA. BASELINE USES MEAN TEACHER METHOD, AND 'UPPERBOUND' DENOTES FULLY SUPERVISED TRAINING ON THE TARGET DOMAIN.

Method	NTIRE2022 → Choledoch		NTIRE2022 → HeiPorSPECTRAL	
	SSIM (%), \uparrow	PSNR (\uparrow)	SSIM (%), \uparrow	PSNR (\uparrow)
Baseline [30]	77.30 \pm 7.22	24.23 \pm 3.57	87.65 \pm 7.96	30.95 \pm 2.29
MCL-SDA [46]	81.72 \pm 6.25	25.96 \pm 2.07	89.87 \pm 8.45	36.12 \pm 2.71
IDM-SDA [48]	82.05 \pm 6.10	26.18 \pm 2.03	90.12 \pm 8.32	36.44 \pm 2.68
Unmix-SDA [51]	82.31 \pm 6.08	26.38 \pm 2.13	90.32 \pm 7.95	38.12 \pm 2.40
PRO-SDA [50]	83.97 \pm 5.62	27.66 \pm 2.10	91.14 \pm 7.42	39.74 \pm 2.14
SpectralAdapt (Ours)	84.26\pm5.12	28.01\pm2.07	95.08\pm4.30	49.12\pm2.02
Upperbound	85.30 \pm 4.16	28.23 \pm 1.28	96.56 \pm 3.22	52.30 \pm 1.90

TABLE III
COMPARISON OF SEGMENTATION PERFORMANCE ACROSS DIFFERENT INPUT MODALITIES ON TWO DOWNSTREAM DATASETS. PA MEASURES OVERALL PIXEL ACCURACY, MPA INDICATES MEAN PER-CLASS ACCURACY, AND mIoU REFLECTS MEAN INTERSECTION OVER UNION.

Dataset	Input	PA (%), \uparrow	MPA (%), \uparrow	mIoU (%), \uparrow
Choledoch	RGB	87.9 \pm 1.0	83.5 \pm 1.5	75.6 \pm 1.2
	HSI	92.3 \pm 0.7	88.1 \pm 1.1	81.7 \pm 1.0
	RS-HSI	90.5\pm0.8	86.0\pm1.2	79.3\pm1.0
HeiPorSPECTRAL	RGB	82.3 \pm 1.3	66.3 \pm 2.0	56.5 \pm 1.6
	HSI	86.7 \pm 1.0	70.2 \pm 1.6	61.7 \pm 1.3
	RS-HSI	84.6\pm1.1	68.7\pm1.8	59.9\pm1.4

Choledoch and HeiPorSPECTRAL datasets, approaching the fully supervised upper bound. These results demonstrate its effectiveness in recovering structurally and spectrally accurate HSI with limited supervision.

Segmentation Accuracy on Downstream Tasks. To further assess the utility of reconstructed hyperspectral images (RS-HSI), we perform semantic segmentation using three input modalities: RGB, raw HSI, and RS-HSI, across two medical benchmarks: Choledoch and HeiPorSPECTRAL. As illustrated in Fig. 5 and detailed in Table III, RS-HSI consistently outperforms RGB inputs across all evaluation metrics, including Pixel Accuracy (PA), Mean Pixel Accuracy (MPA), and Mean Intersection over Union (mIoU), and achieves performance close to that of raw HSI.

In both datasets, the advantages of spectral information are particularly evident in challenging scenarios where RGB fails to capture subtle tissue differences. In the Choledoch dataset, which involves fine-grained glandular structures with minimal visual contrast, RGB-based segmentation often leads to under-segmentation or boundary ambiguity. Similarly, the HeiPorSPECTRAL dataset presents difficulties in delineating organ boundaries under intraoperative conditions, where lighting variability and tissue deformation are common. In both cases, RS-HSI demonstrates improved spatial coherence and reduced fragmentation, leveraging the richer spectral cues restored through reconstruction. Quantitatively, RS-HSI improves mIoU by 2.6% and MPA by 2.5% over RGB on Choledoch, and by 3.4% and 2.4%, respectively, on HeiPorSPECTRAL, while maintaining close alignment with raw HSI predictions. These results underscore the effectiveness of our method in bridging the gap between RGB and real hyperspectral data, enabling more reliable semantic interpretation in clinical scenarios where direct HSI acquisition is constrained.

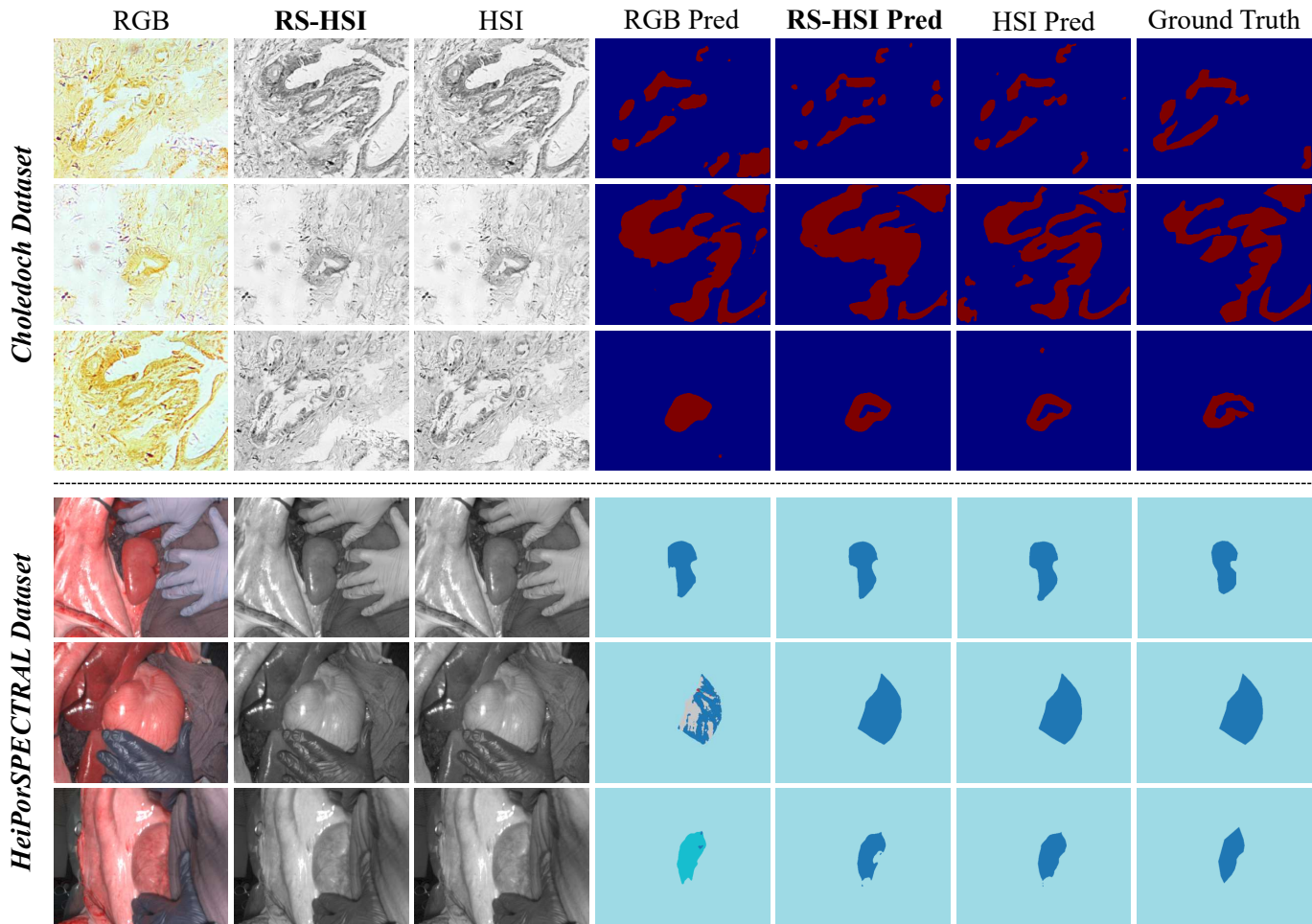


Fig. 5. Qualitative comparison of segmentation results on the Choledoch and HeiPorSPECTRAL datasets using three input modalities: RGB, reconstructed HSI (RS-HSI), and raw HSI. RS-HSI exhibits improved boundary accuracy and spatial consistency over RGB, closely matching the performance of raw HSI. Different colors in the prediction maps denote different semantic classes for each dataset.

F. Ablation Study

To understand the impact of different modules in our approach, we conducted ablation studies to evaluate the contribution of each module and identify the most effective strategies for hyperspectral image reconstruction.

The impact of Masking strategy. To validate our Spectral Density Masking (SDM) method effectiveness, we compared our SDM masking strategy with some common masking techniques, such as block and grid masking. As reported in Table V, SDM consistently outperforms other masking methods by preserving more diverse information across RGB images. Unlike uniform masking, which treats all RGB channels equally, SDM adapts the masking ratio based on the spectral complexity of each channel. This enables the model to place greater emphasis on spectrally dense regions, thereby improving reconstruction quality.

The impact of Module. To validate the effectiveness of different components in the SpectralAdapt method, we conducted a series of ablation studies. The experimental results are summarized in Table IV and visualized in Fig. 6. The results show that SpectralAdapt significantly improves reconstruction performance compared to the baseline. Addi-

TABLE IV

STATISTICAL COMPARISON OF ABLATION RESULTS ON TWO DATASETS USING ONLY 3 (1.5%) LABELED SAMPLES. BASELINE DENOTES THE MEAN TEACHER MODEL TRAINED WITH LABELED SOURCE AND TARGET DATA. SDM AND SERA INDICATE THE SPECTRAL DENSITY MASKING AND SPECTRAL ENDMEMBER REPRESENTATION ALIGNMENT MODULES.

Method	NTIRE2020 → Hyper-Skin		NTIRE2022 → Hyper-Skin	
	SSIM (%), (↑)	PSNR (↑)	SSIM (%), (↑)	PSNR (↑)
Baseline	85.30±9.69	23.23±1.57	85.65±7.96	27.95±2.29
Baseline+SDM	87.86±8.43	27.23±2.68	88.11±8.71	28.69±2.40
Baseline+SERA	89.36±8.40	27.62±2.68	89.52±8.55	29.01±2.43
Baseline+SDM+SERA (Ours)	90.24±7.72	28.78±2.07	91.55±7.16	30.72±2.06

TABLE V

STATISTICAL COMPARISON OF OUR ABLATION STUDIES ON TWO DATASETS WITH 3 (1.5%) LABELED HUMAN SAMPLES.

Method	NTIRE2020 → Hyper-Skin		NTIRE2022 → Hyper-Skin	
	SSIM (%), (↑)	PSNR (↑)	SSIM (%), (↑)	PSNR (↑)
Baseline	85.30±9.69	23.23±1.57	85.65±7.96	27.95±2.29
Baseline+Uniform Block Masking	86.43±9.30	25.20±1.43	86.82±7.96	28.12±2.05
Baseline+Uniform Grid Masking	87.15±8.89	25.78±2.03	87.94±9.71	28.30±2.75
Baseline+Spectral Density Masking	87.86±8.43	27.23±2.68	88.11±8.71	28.69±2.40



Fig. 6. Error map visual comparisons of predictions using different modules in different subject postures.

TABLE VI
PERFORMANCE COMPARISON UNDER DIFFERENT MASKING RATES USING SPECTRAL DENSITY MASKING (SDM).

Masking Rate (%)	NTIRE2020 → Hyper-Skin		NTIRE2022 → Hyper-Skin	
	SSIM (%), \uparrow	PSNR (\uparrow)	SSIM (%), \uparrow	PSNR (\uparrow)
10	88.92 \pm 8.40	25.85 \pm 1.93	89.65 \pm 8.92	27.44 \pm 2.12
30	89.45 \pm 8.05	26.71 \pm 2.01	90.52 \pm 8.65	28.32 \pm 2.38
50	90.01 \pm 7.81	27.55 \pm 2.14	91.10 \pm 7.96	29.11 \pm 2.47
70	90.24\pm7.72	28.78\pm2.07	91.55\pm7.16	30.72\pm2.06
90	89.10 \pm 8.52	26.10 \pm 2.26	89.42 \pm 8.30	27.86 \pm 2.23

tional improvements are achieved by integrating the Spectral Density Masking (SDM) module, which adaptively retains information-rich spectral regions by accounting for the varying complexity of RGB channels, and the Spectral Endmember Representation Alignment (SERA) module, which promotes spectral consistency by aligning predictions with physically interpretable spectral prototypes. The combined SpectralAdapt method, equipped with both SDM and SERA, achieves the best overall performance, demonstrating its effectiveness in improving human hyperspectral image reconstruction under the semi-supervised setting.

The impact of Hyperparameter. To evaluate the robustness and tunability of our method, we perform a comprehensive sensitivity analysis on two key training factors: the loss weights λ and the masking rate r in our masking strategy.

The hyperparameter λ_{sup} balances the contribution of the pixel-wise \mathcal{L}_1 loss and perceptual $\mathcal{L}_{\text{SSIM}}$ loss in the supervised branch, while λ_{un} controls the trade-off between consistency loss and spectral endmember alignment in the unsupervised branch. As illustrated in Fig. 7, our method maintains consistently strong SSIM performance across various combinations of loss weights. The best result is observed when $\lambda_{\text{sup}} = 0.4$ and $\lambda_{\text{un}} = 0.3$, suggesting that placing more emphasis on structural similarity and spectral alignment benefits hyperspectral reconstruction.

We also analyze the effect of different masking rates in SDM, which determines the proportion of input pixels occluded during training. As reported in Table VI, a bell-shaped trend is observed: both low masking rates (e.g., 10%) and high masking rates (e.g., 90%) lead to suboptimal performance due to under-regularization and excessive information loss,

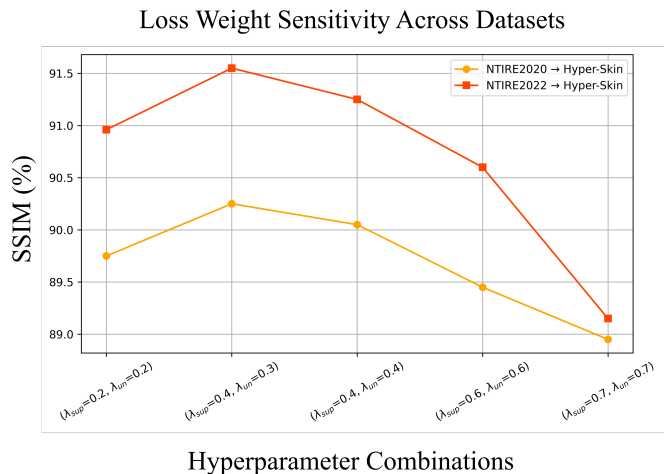


Fig. 7. Sensitivity analysis of loss weight hyperparameters λ_{sup} and λ_{un} on two semi-supervised domain adaptation tasks. Each point represents a specific combination of supervised and unsupervised loss weights, with SSIM used to evaluate reconstruction performance.

respectively. The optimal masking rate of 70% effectively balances informativeness and regularization, further improving the model’s generalization ability in the semi-supervised domain adaptation setting.

VI. CONCLUSION

In this work, we tackled the challenging problem of semi-supervised domain adaptation (SSDA) for human hyperspectral image (HSI) reconstruction. Our approach overcomes the challenges posed by spectral distribution imbalance and cross-domain distributional shifts. To address these issues, we propose the SpectralAdapt method with spectral prior guidance for HSI reconstruction based on the Mean Teacher structure, which incorporates spectral knowledge into the learning process by jointly leveraging spectral density masking and endmember-based alignment. Specifically, the Spectral Density Masking (SDM) module dynamically adjusts masking ratios based on the spectral complexity of each RGB channel, encouraging the model to focus on informative spectral regions and better capture inter-channel dependencies. In addition, the Spectral Endmember Representation Alignment (SERA) module utilizes physically interpretable endmembers derived from labeled data to guide the model toward domain-invariant spectral representations. These components enable the model to effectively exploit both limited labeled and abundant unlabeled data across domains. Extensive experiments on benchmark datasets validate the effectiveness of the proposed approach, demonstrating improvements in spectral fidelity, cross-domain generalization, and training robustness. The results underscore the potential of SSDA as a practical solution for human-centered hyperspectral imaging in clinical and physiological settings.

REFERENCES

- [1] M. J. Khan, H. S. Khan, A. Yousaf, K. Khurshid, and A. Abbas, “Modern trends in hyperspectral image analysis: A review,” *Ieee Access*, vol. 6, pp. 14 118–14 129, 2018.

- [2] S. Peyghambari and Y. Zhang, "Hyperspectral remote sensing in lithological mapping, mineral exploration, and environmental geology: an updated review," *Journal of Applied Remote Sensing*, vol. 15, no. 3, pp. 031 501–031 501, 2021.
- [3] A. Nisha and A. Anitha, "Current advances in hyperspectral remote sensing in urban planning," in *2022 Third International Conference on intelligent computing instrumentation and control technologies (ICI-CICT)*. IEEE, 2022, pp. 94–98.
- [4] M. Barberio, S. Benedicenti, M. Pizzicannella, E. Felli, T. Collins, B. Jansen-Winkel, J. Marescaux, M. G. Viola, and M. Diana, "Intra-operative guidance using hyperspectral imaging: a review for surgeons," *Diagnostics*, vol. 11, no. 11, p. 2066, 2021.
- [5] R. Leon, B. Martinez-Vega, H. Fabelo, S. Ortega, V. Melian, I. Castaño, G. Carretero, P. Almeida, A. Garcia, E. Quevedo *et al.*, "Non-invasive skin cancer diagnosis using hyperspectral imaging for in-situ clinical support," *Journal of clinical medicine*, vol. 9, no. 6, p. 1662, 2020.
- [6] I. H. Aboughaleb, M. H. Aref, and Y. H. El-Sharkawy, "Hyperspectral imaging for diagnosis and detection of ex-vivo breast cancer," *Photodiagnosis and Photodynamic Therapy*, vol. 31, p. 101922, 2020.
- [7] M. H. Skjelvareid, K. Heia, S. H. Olsen, and S. K. Stormo, "Detection of blood in fish muscle by constrained spectral unmixing of hyperspectral images," *Journal of Food Engineering*, vol. 212, pp. 252–261, 2017.
- [8] C. Sicher, R. Rutkowski, S. Lutze, S. von Podewils, T. Wild, M. Kretching, and G. Daeschlein, "Hyperspectral imaging as a possible tool for visualization of changes in hemoglobin oxygenation in patients with deficient hemodynamics—proof of concept," *Biomedical Engineering/Biomedizinische Technik*, vol. 63, no. 5, pp. 609–616, 2018.
- [9] B. Arad, R. Timofte, R. Yabel, N. Morag, A. Bernat, Y. Cai, J. Lin, Z. Lin, H. Wang, Y. Zhang *et al.*, "Ntire 2022 spectral recovery challenge and data set," in *Proceedings of the IEEE/CVF Conference on Computer Vision and Pattern Recognition*, 2022, pp. 863–881.
- [10] P. C. Ng, Z. Chi, Y. Verdie, J. Lu, and K. N. Plataniotis, "Hyper-skin: a hyperspectral dataset for reconstructing facial skin-spectra from rgb images," *Advances in Neural Information Processing Systems*, vol. 36, 2024.
- [11] M. Zhang, C. Zhang, Q. Zhang, J. Guo, X. Gao, and J. Zhang, "Essaformer: Efficient transformer for hyperspectral image super-resolution," in *Proceedings of the IEEE/CVF International Conference on Computer Vision*, 2023, pp. 23 073–23 084.
- [12] A. Brorsson, M. Nordberg, and D. Gustafsson, "Reconstruction of cassiraman images with machine-learning," in *Proceedings of the IEEE/CVF Conference on Computer Vision and Pattern Recognition*, 2021, pp. 4388–4395.
- [13] Q. Zhang, R. Plemmons, D. Kittle, D. Brady, and S. Prasad, "Reconstructing and segmenting hyperspectral images from compressed measurements," in *2011 3rd Workshop on Hyperspectral Image and Signal Processing: Evolution in Remote Sensing (WHISPERS)*. IEEE, 2011, pp. 1–4.
- [14] Y. Li, W. Xie, and H. Li, "Hyperspectral image reconstruction by deep convolutional neural network for classification," *Pattern Recognition*, vol. 63, pp. 371–383, 2017.
- [15] L. Wang, C. Sun, Y. Fu, M. H. Kim, and H. Huang, "Hyperspectral image reconstruction using a deep spatial-spectral prior," in *Proceedings of the IEEE/CVF Conference on Computer Vision and Pattern Recognition*, 2019, pp. 8032–8041.
- [16] Y. Chang, L. Yan, H. Fang, S. Zhong, and W. Liao, "Hsi-denet: Hyperspectral image restoration via convolutional neural network," *IEEE Transactions on Geoscience and Remote Sensing*, vol. 57, no. 2, pp. 667–682, 2018.
- [17] Y. Cai, J. Lin, X. Hu, H. Wang, X. Yuan, Y. Zhang, R. Timofte, and L. Van Gool, "Mask-guided spectral-wise transformer for efficient hyperspectral image reconstruction," in *Proceedings of the IEEE/CVF Conference on Computer Vision and Pattern Recognition*, 2022, pp. 17 502–17 511.
- [18] —, "Coarse-to-fine sparse transformer for hyperspectral image reconstruction," in *European conference on computer vision*. Springer, 2022, pp. 686–704.
- [19] A. Chakrabarti and T. Zickler, "Statistics of real-world hyperspectral images," in *CVPR 2011*. IEEE, 2011, pp. 193–200.
- [20] F. Yasuma, T. Mitsunaga, D. Iso, and S. K. Nayar, "Generalized assorted pixel camera: postcapture control of resolution, dynamic range, and spectrum," *IEEE transactions on image processing*, vol. 19, no. 9, pp. 2241–2253, 2010.
- [21] W. G. C. Bandara, J. M. J. Valanarasu, and V. M. Patel, "Hyperspectral pansharpening based on improved deep image prior and residual reconstruction," *IEEE Transactions on Geoscience and Remote Sensing*, vol. 60, pp. 1–16, 2021.
- [22] Y. Zhang, W. Li, W. Jia, M. Zhang, R. Tao, and S. Liang, "Cross-domain hyperspectral image classification based on bi-directional domain adaptation," *IEEE Transactions on Circuits and Systems for Video Technology*, 2025.
- [23] Y. Wang, J. Yin, W. Li, P. Frossard, R. Yang, and J. Shen, "Ssda3d: Semi-supervised domain adaptation for 3d object detection from point cloud," in *Proceedings of the AAAI Conference on Artificial Intelligence*, vol. 37, no. 3, 2023, pp. 2707–2715.
- [24] S. Feng, J. Zhang, Y. Fan, X. Liu, C. Zhao, W. Li, and R. Tao, "Cross-domain few-shot learning method based on fractional domain information for hyperspectral image multi-class change detection," *IEEE Transactions on Circuits and Systems for Video Technology*, 2025.
- [25] L. Wang and K.-J. Yoon, "Semi-supervised student-teacher learning for single image super-resolution," *Pattern Recognition*, vol. 121, p. 108206, 2022.
- [26] Z. Fang, J. Lu, F. Liu, and G. Zhang, "Semi-supervised heterogeneous domain adaptation: Theory and algorithms," *IEEE Transactions on Pattern Analysis and Machine Intelligence*, vol. 45, no. 1, pp. 1087–1105, 2022.
- [27] B. Lucas, C. Pelletier, D. Schmidt, G. I. Webb, and F. Petitjean, "A bayesian-inspired, deep learning-based, semi-supervised domain adaptation technique for land cover mapping," *Machine Learning*, vol. 112, no. 6, pp. 1941–1973, 2023.
- [28] H. Guan and M. Liu, "Domain adaptation for medical image analysis: a survey," *IEEE Transactions on Biomedical Engineering*, vol. 69, no. 3, pp. 1173–1185, 2021.
- [29] S. Ben-David, J. Blitzer, K. Crammer, A. Kulesza, F. Pereira, and J. W. Vaughan, "A theory of learning from different domains," *Machine learning*, vol. 79, pp. 151–175, 2010.
- [30] A. Tarvainen and H. Valpola, "Mean teachers are better role models: Weight-averaged consistency targets improve semi-supervised deep learning results," *Advances in neural information processing systems*, vol. 30, 2017.
- [31] F. A. Kruse, A. Lefkoff, y. J. Boardman, K. Heidebrecht, A. Shapiro, P. Barloon, and A. Goetz, "The spectral image processing system (sips)—interactive visualization and analysis of imaging spectrometer data," *Remote sensing of environment*, vol. 44, no. 2–3, pp. 145–163, 1993.
- [32] J. Zhang, R. Su, Q. Fu, W. Ren, F. Heide, and Y. Nie, "A survey on computational spectral reconstruction methods from rgb to hyperspectral imaging," *Scientific reports*, vol. 12, no. 1, p. 11905, 2022.
- [33] K. Yorimoto and X.-H. Han, "Hypermixnet: hyperspectral image reconstruction with deep mixed network from a snapshot measurement," in *Proceedings of the IEEE/CVF International Conference on Computer Vision*, 2021, pp. 1184–1193.
- [34] M. Li, Y. Fu, J. Liu, and Y. Zhang, "Pixel adaptive deep unfolding transformer for hyperspectral image reconstruction," in *Proceedings of the IEEE/CVF International Conference on Computer Vision*, 2023, pp. 12 959–12 968.
- [35] L. Yan, X. Wang, M. Zhao, M. Kaloorazi, J. Chen, and S. Rahardja, "Reconstruction of hyperspectral data from rgb images with prior category information," *IEEE Transactions on Computational Imaging*, vol. 6, pp. 1070–1081, 2020.
- [36] Y. Zhao, L.-M. Po, T. Lin, Q. Yan, W. Liu, and P. Xian, "Hsgan: Hyperspectral reconstruction from rgb images with generative adversarial network," *IEEE Transactions on Neural Networks and Learning Systems*, 2023.
- [37] Y. Chen, W. Lai, W. He, X.-L. Zhao, and J. Zeng, "Hyperspectral compressive snapshot reconstruction via coupled low-rank subspace representation and self-supervised deep network," *IEEE Transactions on Image Processing*, 2024.
- [38] Y. Chen, F. Yuan, W. Lai, J. Zeng, W. He, and Q. Huang, "Low-rank tensor meets deep prior: Coupling model-driven and data-driven methods for hyperspectral image reconstruction," *IEEE Transactions on Circuits and Systems for Video Technology*, 2025.
- [39] H. Chen, W. Zhao, T. Xu, G. Shi, S. Zhou, P. Liu, and J. Li, "Spectral-wise implicit neural representation for hyperspectral image reconstruction," *IEEE Transactions on Circuits and Systems for Video Technology*, 2023.
- [40] J. Xue, Y.-Q. Zhao, Y. Bu, W. Liao, J. C.-W. Chan, and W. Philips, "Spatial-spectral structured sparse low-rank representation for hyperspectral image super-resolution," *IEEE Transactions on Image Processing*, vol. 30, pp. 3084–3097, 2021.
- [41] S. Zhang, L. Wang, L. Zhang, and H. Huang, "Learning tensor low-rank prior for hyperspectral image reconstruction," in *Proceedings of the IEEE/CVF conference on computer vision and pattern recognition*, 2021, pp. 12 006–12 015.

- [42] X. Yang, Z. Song, I. King, and Z. Xu, "A survey on deep semi-supervised learning," *IEEE transactions on knowledge and data engineering*, vol. 35, no. 9, pp. 8934–8954, 2022.
- [43] J. E. Van Engelen and H. H. Hoos, "A survey on semi-supervised learning," *Machine learning*, vol. 109, no. 2, pp. 373–440, 2020.
- [44] Z. Feng, S. Tong, S. Yang, X. Zhang, and L. Jiao, "Pseudo-label-assisted subdomain adaptation for hyperspectral image classification," *IEEE Transactions on Circuits and Systems for Video Technology*, vol. 34, no. 6, pp. 4729–4744, 2023.
- [45] D. Berthelot, R. Roelofs, K. Sohn, N. Carlini, and A. Kurakin, "Adamatch: A unified approach to semi-supervised learning and domain adaptation," in *Proceedings of the 10th International Conference on Learning Representations (ICLR)*, 2022.
- [46] Z. Yan, Y. Wu, G. Li, Y. Qin, X. Han, and S. Cui, "Multi-level consistency learning for semi-supervised domain adaptation," in *Proceedings of the Thirty-First International Joint Conference on Artificial Intelligence (IJCAI)*. IJCAI, 2022, pp. 1530–1536.
- [47] Q. Zhou, Z. Feng, Q. Gu, J. Pang, G. Cheng, X. Lu, J. Shi, and L. Ma, "Context-aware mixup for domain adaptive semantic segmentation," *IEEE Transactions on Circuits and Systems for Video Technology*, vol. 33, no. 2, pp. 804–817, 2022.
- [48] J. Li, G. Li, and Y. Yu, "Inter-domain mixup for semi-supervised domain adaptation," *Pattern Recognition*, vol. 146, p. 110023, 2024.
- [49] N. Ma, H. Wang, Z. Zhang, S. Zhou, H. Chen, and J. Bu, "Source-free semi-supervised domain adaptation via progressive mixup," *Knowledge-Based Systems*, vol. 262, p. 110208, 2023.
- [50] X. Huang, C. Zhu, and W. Chen, "Semi-supervised domain adaptation via prototype-based multi-level learning," in *Proceedings of the 32nd International Joint Conference on Artificial Intelligence (IJCAI)*. IJCAI, 2023, pp. 884–892.
- [51] R. K. Baghbaderani, Y. Qu, and H. Qi, "Unsupervised hyperspectral image domain adaptation through unmixing-based domain alignment," in *IGARSS 2023-2023 IEEE International Geoscience and Remote Sensing Symposium*. IEEE, 2023, pp. 5906–5909.
- [52] Y. Zhang, J. Shi, J. Wang, Y. Zong, W. Zheng, and G. Zhao, "Maskfusionnet: A dual-stream fusion model with masked pre-training mechanism for rppg measurement," *IEEE Transactions on Circuits and Systems for Video Technology*, 2024.
- [53] S.-H. Bae and M. Kim, "A dct-based total jnd profile for spatiotemporal and foveated masking effects," *IEEE Transactions on Circuits and Systems for Video Technology*, vol. 27, no. 6, pp. 1196–1207, 2016.
- [54] T. Chen, X. Ma, X. Liu, W. Wang, R. Feng, J. Chen, C. Yuan, W. Lu, D. Z. Chen, and J. Wu, "Multi-view learning with feature level fusion for cervical dysplasia diagnosis," in *Medical Image Computing and Computer Assisted Intervention*. Springer, 2019, pp. 329–338.
- [55] B. Somers, G. P. Asner, L. Tits, and P. Coppin, "Endmember variability in spectral mixture analysis: A review," *Remote Sensing of Environment*, vol. 115, no. 7, pp. 1603–1616, 2011.
- [56] A. Plaza and C.-I. Chang, "Impact of initialization on design of endmember extraction algorithms," *IEEE Transactions on Geoscience and Remote Sensing*, vol. 44, no. 11, pp. 3397–3407, 2006.
- [57] Z. Wang, A. C. Bovik, H. R. Sheikh, and E. P. Simoncelli, "Image quality assessment: from error visibility to structural similarity," *IEEE transactions on image processing*, vol. 13, no. 4, pp. 600–612, 2004.
- [58] B. Arad, R. Timofte, O. Ben-Shahar, Y.-T. Lin, and G. D. Finlayson, "Ntire 2020 challenge on spectral reconstruction from an rgb image," in *Proceedings of the IEEE/CVF conference on computer vision and pattern recognition workshops*, 2020, pp. 446–447.
- [59] Q. Zhang, Q. Li, G. Yu, L. Sun, M. Zhou, and J. Chu, "A multidimensional choledoch database and benchmarks for cholangiocarcinoma diagnosis," *IEEE access*, vol. 7, pp. 149 414–149 421, 2019.
- [60] A. Studier-Fischer, S. Seidlitz, J. Sellner, M. Bressan, B. Özdemir, L. Ayala, J. Odenthal, S. Knoedler, K.-F. Kowalewski, C. M. Haney *et al.*, "Heiporspectral-the heidelberg porcine hyperspectral imaging dataset of 20 physiological organs," *Scientific Data*, vol. 10, no. 1, p. 414, 2023.
- [61] Y. Cai, J. Lin, Z. Lin *et al.*, "Mst++: Multi-stage Spectral-wise Transformer for Efficient Spectral Reconstruction," in *Proceedings of the IEEE/CVF Conference on Computer Vision and Pattern Recognition*, 2022, pp. 745–755.
- [62] A. Hore and D. Ziou, "Image quality metrics: Psnr vs. ssim," in *2010 20th international conference on pattern recognition*. IEEE, 2010, pp. 2366–2369.
- [63] J. Long, E. Shelhamer, and T. Darrell, "Fully convolutional networks for semantic segmentation," in *Proceedings of the IEEE conference on computer vision and pattern recognition*, 2015, pp. 3431–3440.
- [64] M. Everingham, L. Van Gool, C. K. Williams, J. Winn, and A. Zisserman, "The pascal visual object classes (voc) challenge," *International journal of computer vision*, vol. 88, pp. 303–338, 2010.
- [65] O. Ronneberger, P. Fischer, and T. Brox, "U-net: Convolutional networks for biomedical image segmentation," in *International Conference on Medical image computing and computer-assisted intervention*. Springer, 2015, pp. 234–241.
- [66] V. Cheplygina, M. De Bruijne, and J. P. Pluim, "Not-so-supervised: a survey of semi-supervised, multi-instance, and transfer learning in medical image analysis," *Medical image analysis*, vol. 54, pp. 280–296, 2019.
- [67] R. Jiao, Y. Zhang, L. Ding, B. Xue, J. Zhang, R. Cai, and C. Jin, "Learning with limited annotations: a survey on deep semi-supervised learning for medical image segmentation," *Computers in Biology and Medicine*, vol. 169, p. 107840, 2024.